SUN2 regulates mitotic duration in response to extracellular matrix rigidity

Nejma Belaadi[a,b,1] 📷, Lydia Pernet[a] 📷, Julien Aureille[a] 📷, Gilliane Chadeuf[b], Marc Rio[b] 📷, Nathalie Vaillant[b], Elisa Vitiello[c], Laurence Lafanechère[a] 📷, Gervaise Loirand[b], and Christophe Guilluy[a,d,1]

How cells adjust their growth to the spatial and mechanical constraints of their surrounding environment is central to many aspects of biology. Here, we examined how extracellular matrix (ECM) rigidity affects cell division. We found that cells divide more rapidly when cultured on rigid substrates. While we observed no effect of ECM rigidity on rounding or postmitotic spreading duration, we found that changes in matrix stiffness impact mitosis progression. We noticed that ECM elasticity up-regulates the expression of the linker of nucleoskeleton and cytoskeleton (LINC) complex component SUN2, which in turn promotes metaphase-to-anaphase transition by acting on mitotic spindle formation, whereas when cells adhere to soft ECM, low levels of SUN2 expression perturb astral microtubule organization and delay the onset of anaphase.

mitosis | nucleus | LINC | mechanotransduction | matrix

Many aspects of cell growth are regulated by the spatial and mechanical properties of their microenvironment. Using experimental approaches to modulate the spatial constraints that cells experience in culture, studies showed that imposed boundary conditions can deeply influence cell proliferation. For example, restricting cell height or lateral expansion hinders mitosis progression (1, 2), while constraining cell shape during interphase impacts cell-cycle progression, in particular by regulating G1–S transition (3, 4). In parallel to spatial constraints, mechanical forces influence cell proliferation. It is well-appreciated that applying mechanical tension on cells promotes cell-cycle progression, by affecting the expression of cell-cycle checkpoint regulators (5–7). Consistent with that, increasing the elasticity of the substrates, which stimulates cell-generated tension, promotes cell-cycle progression (8, 9). An exacerbated cellular response to tension causes excessive proliferation, which can contribute critically to pathological tissue remodeling (10) and compromise tissue homeostasis (11), indicating that mechanical tension, either applied externally or generated by the cell's own cytoskeleton, is a key regulator of cell-cycle progression. While the impact of matrix elasticity on cell-cycle progression during interphase has been extensively studied, its consequence on mitosis has been less documented.

As cells progress in mitosis, they drastically change their shape to accommodate the cellular machinery and allow chromosome segregation. These changes are mediated by the cytoskeleton and associated with adhesion disassembly when cells enter prophase. Concomitantly, a contractile actomyosin cortex forms and associates with the cellular membrane, while the microtubule network reorganizes to form a bipolar spindle whose associated molecular motors allow chromosome segregation (12). Parallel to this cytoskeletal remodeling, the nuclear envelope of metazoan cells breaks down (13), a feature that comprises distinct steps including disassembly of the nuclear pore complex (NPC), lamina depolymerization and removal of nuclear membranes from chromatin (13). Whereas the nuclear envelope disassembles during mitosis, work shows that some nuclear envelope proteins contribute to mitosis progression. For example, lamin B (14) or some nucleoporins (13, 15, 16), that is, the components of the NPC, promote mitotic spindle formation following nuclear envelope breakdown (NEBD). Additionally, studies reported that the proteins belonging to the linker of nucleoskeleton and cytoskeleton (LINC) complex participate in the initial steps of mitosis via their connection with microtubule-associated motors (17, 18).

In this study, we cultured cells on matrix with various elasticity and investigated the consequences for mitosis duration. We found that cells cultured on more rigid matrix complete mitosis more quickly compared with cells on soft substrates. We observed that increasing matrix rigidity during interphase up-regulates the expression of the LINC component Sad1 and UNC84 domain containing 2 (SUN2), which in turn accelerates mitosis by promoting mitotic spindle formation and metaphase-to-anaphase transition.

Significance

Under physiological conditions, there are numerous signals perceived by cells that influence their growth. Here, we observed that the mechanical properties of the cellular microenvironment control the progression of cell division. We found that cells divide more rapidly when cultured on substrates with increasing rigidity. This mechanism involves the nuclear protein SUN2, whose expression is up-regulated by matrix rigidity and in turn accelerates mitosis by promoting metaphase-to-anaphase transition.

Author affiliations: [a]Institute for Advanced Biosciences, Université Grenoble Alpes, CNRS UMR5309, INSERM U1209, 38700 La Tronche, France; [b]Nantes Université, CHU Nantes, CNRS, INSERM, l'institut du thorax, F-44000 Nantes, France; [c]Laboratoire Interdisciplinaire de Physique, CNRS UMR 5588, Université Grenoble Alpes, 38000 Grenoble, France; and [d]Department of Molecular Biomedical Sciences, College of Veterinary Medicine, North Carolina State University, Raleigh, NC 27606

[1]To whom correspondence may be addressed. Email: belaadi.nejma@gmail.com or christophe.guilluy@inserm.fr.

Results

Matrix Elasticity Regulates Mitosis Duration. In order to evaluate the effect of extracellular matrix (ECM) rigidity on cell division, we cultured A7R5 cells (vascular smooth muscle cells) on soft (1 kPa) or stiff (50 kPa) polyacrylamide substrates coated with collagen I and measured mitosis duration (Fig. 1A).

We observed that cells divide more rapidly on stiff surfaces compared with cells plated on soft substrates (Fig. 1B). A similar change in mitosis duration was observed when we cultured mouse embryonic fibroblasts (MEFs) or HeLa cells on 1- or 50-kPa ECM (Fig. 1B). Interestingly, we observed a gradual decrease in mitosis duration as we cultured cells on more rigid ECM (*SI Appendix*, Fig. 1A). However, no significant change
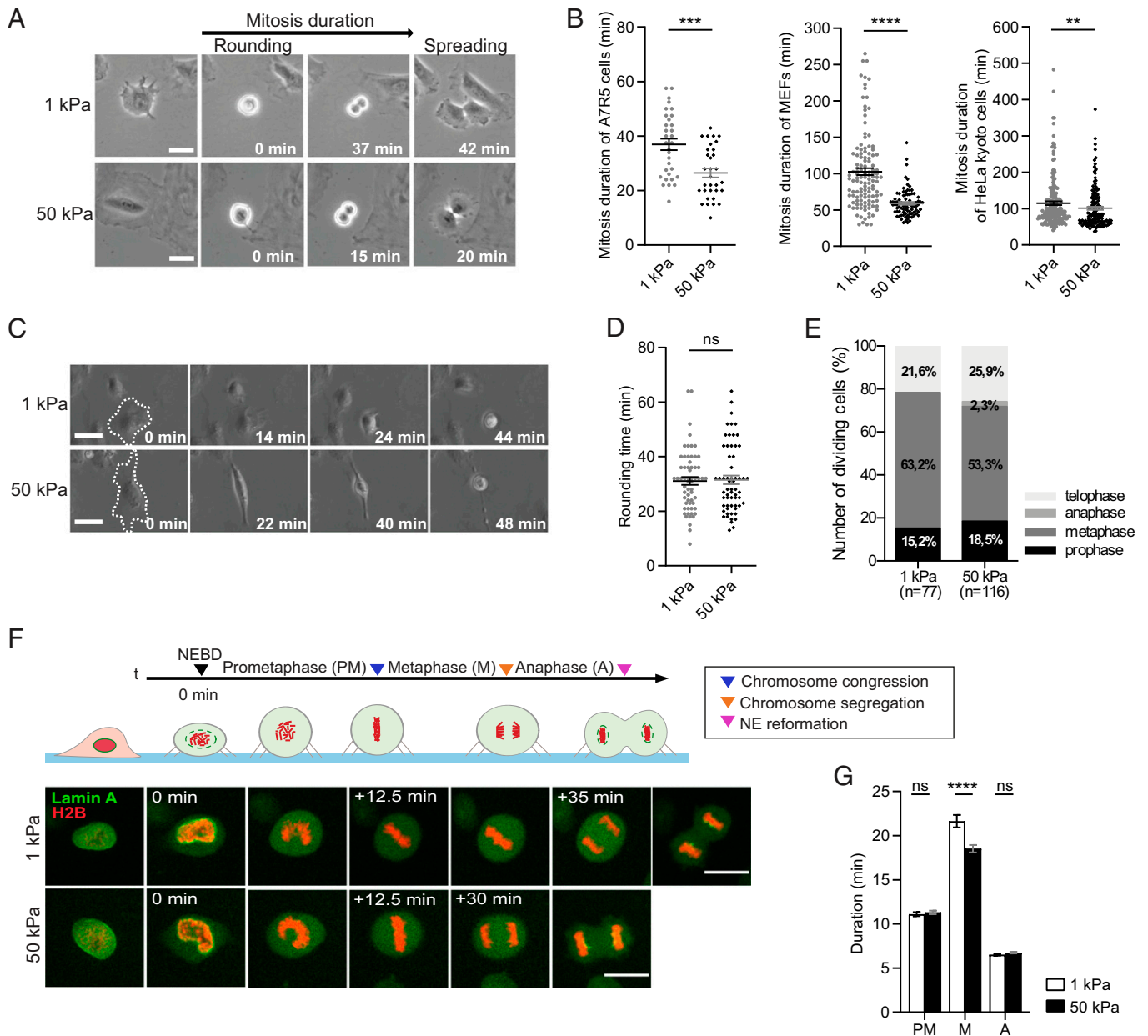
Fig. 1. ECM rigidity regulates mitosis duration. (A) A7R5 cells were cultured on soft (1 kPa) and stiff (50 kPa) polyacrylamide hydrogels coated with collagen I. Cells were imaged using phase-contrast microscopy and the duration of mitosis was calculated as the elapsed time between the onset of rounding to the first image demonstrating cytokinesis and postmitotic spreading. (Scale bars, 10 μm.) (B) Mitosis duration was quantified for A7R5 cells (n = 32 cells for 1 kPa; n = 32 cells for 50 kPa; from three independent experiments; ***P < 0.001, Mann–Whitney U test), MEFs (n = 121 cells for 1 kPa; n = 85 cells for 50 kPa; from three independent experiments; ****P < 0.0001, Mann–Whitney U test), and HeLa Kyoto cells (n = 193 cells for 1 kPa; n = 151 cells for 50 kPa; from three independent experiments; **P < 0.01, Mann–Whitney U test) (error bars indicate means ± SEM). (C) A7R5 cells were cultured on soft (1 kPa) and stiff (50 kPa) polyacrylamide hydrogels coated with collagen I. Elapsed time from initial cell margin retraction to complete rounding was calculated. (Scale bars, 10 μm.) (D) Rounding duration was quantified for A7R5 cells (n = 61 cells for each condition from three independent experiments; error bars indicate means ± SEM; ns, not significant; Mann–Whitney U test). (E) HeLa Kyoto cells cultured on soft (1 kPa) and stiff (50 kPa) polyacrylamide hydrogels were fixed and the percentage of cells undergoing, respectively, prophase, metaphase, anaphase, and telophase was quantified (n = 77 mitotic cells for 1 kPa; n = 116 mitotic cells for 50 kPa; 30 microscopic fields were taken per condition from one experiment). (F) HeLa Kyoto EGFP-LaminA/H2B-mCherry cells cultured on soft (1 kPa) and stiff (50 kPa) polyacrylamide hydrogels were imaged using live confocal microscopy. The duration of each stage of mitosis was calculated using the breakdown of the nuclear envelope (NEBD), shown by lamin A staining (green), as the starting point. The diagram represents the method used to calculate the phases of mitosis. (Scale bars, 20 μm.) (G) Corresponding quantifications of mitosis phase duration: prometaphase (PM), metaphase (M), and anaphase (A) (n = 217 cells for 1 kPa and n = 271 cells for 50 kPa from three independent experiments; error bars indicate means ± SEM; ns, not significant; ****P < 0.0001, two-way ANOVA, Sidak's multiple-comparisons posttest).

in mitosis duration was observed when substrates more rigid than 12 kPa were used (*SI Appendix*, Fig. 1*A*), suggesting that ECM rigidity affects mitotic progression within a range of rigidity before reaching a plateau.

Since ECM rigidity affects integrin-based adhesion maturation, we investigated whether ECM rigidity impacts deadhesion duration. We measured the elapsed time from initial retraction of the cell margin to complete rounding, and did not observe any difference whether cells were cultured on soft or stiff ECM (Fig. 1 *C* and *D*). Similarly, we observed no difference in postmitotic spreading, which started less than 5 min following anaphase regardless of the ECM stiffness (Fig. 1*A*). Next, we investigated whether changes in ECM rigidity could regulate the progression of specific cell-division steps. We fixed actively dividing cells and quantified the percentage of cells undergoing prophase, metaphase, anaphase, or telophase, respectively. We observed an increased proportion of cells in metaphase when cells were cultured on softer ECM (Fig. 1*E*). To explore this further, we imaged HeLa cells stably expressing fluorescent lamin A and histone 2B using spinning disk confocal microscopy. We monitored NEBD, chromosome congression, and chromosome segregation to quantify the duration of each phase in cells dividing on soft or stiff ECM (Fig. 1*F*). We found that cells on soft ECM undergo a longer metaphase compared with cells on more rigid substrates (Fig. 1 *F* and *G*), while the progression of the other phases of mitosis was not affected. This indicates that low ECM stiffness causes a metaphase delay that results in overall longer mitosis (*SI Appendix*, Fig. 1*B*).

SUN2 Level of Expression Affects Mitosis Duration. Force-bearing cytoskeletal elements that transmit and/or transduce mechanical stress have been shown to play a key role in mediating the effect of ECM rigidity on cell behavior (19). To identify the cytoskeletal processes that regulate mitosis duration in response to changes in ECM rigidity, we synchronized in mitosis using the Eg5 inhibitor *S*-trityl-L-cysteine (STC) and compared the detergent-insoluble proteomic content of cells cultured on soft or stiff ECM (Fig. 2*A*). Among the differences, we observed a change in SUN2 expression between soft and stiff ECM. SUN2 is an inner nuclear membrane (INM) protein that belongs to the LINC complex and interacts with nesprins to connect the cytoskeleton to the lamina. We found that cells express an increased amount of SUN2 when plated on more rigid ECM (Fig. 2 *A–D*). We next looked at mitosis duration in cells depleted of SUN2 and found that SUN2 depletion caused a significant increase in mitosis duration (Fig. 2 *E* and *F* and *SI Appendix*, Fig. 2*A*), which was rescued when we overexpressed a small interfering RNA (siRNA)–resistant truncated version of SUN2 (DS-SUN2-GFP [green fluorescent protein]; *SI Appendix*, Fig. 2*B*). Interestingly, SUN1 depletion had no effect on mitosis progression (*SI Appendix*, Fig. 2*C*). Cells depleted for SUN2 and plated on 50-kPa ECM completed mitosis in an average duration similar to cells transfected with control siRNA and plated on 1-kPa (Fig. 2*F*), indicating that SUN2 participates in the effect of ECM rigidity on mitosis duration; however, we cannot rule out that additional mechanisms may contribute to the effect of matrix elasticity on mitosis.

We next explored if this increase in SUN2 expression was the consequence of an increase in *SUN2* transcription or a decrease in SUN2 protein degradation. Using real-time qPCR, we examined *SUN2* messenger RNA expression, and observed no significant changes in response to ECM rigidity (*SI Appendix*, Fig. 2*D*). To investigate SUN2 degradation, we blocked protein synthesis using cycloheximide (CHX) and analyzed SUN2 expression using immunofluorescence (IF) (Fig. 2 *G* and *H*) and Western blot (WB) (*SI Appendix*, Fig. 2 *E* and *F*). Following CHX treatment,

SUN2 degradation was reduced when cells were cultured on rigid substrate (Fig. 2*H* and *SI Appendix*, Fig. 2*F*), indicating that SUN2 stability increases with ECM rigidity. As cells develop more actomyosin contractility when they are cultured on rigid substrates (20), we hypothesized that SUN2-increased stability observed on rigid substrates may be related to actomyosin tension. Consistent with this, we observed that inhibiting myosin 2 with blebbistatin decreased SUN2 expression (*SI Appendix*, Fig. 2*H*) and SUN2 degradation was faster in cells treated with blebbistatin (85 versus 68% degradation in nontreated cells after 24 h of CHX treatment; *SI Appendix*, Fig. 2*I*).

SUN2 Knockdown Delays Metaphase Completion. We next investigated how SUN2 level of expression regulates mitosis progression and followed cell division in cells expressing fluorescent lamin A and histone 2B using spinning disk confocal microscopy. We found that SUN2 depletion significantly delayed metaphase completion (Fig. 3 *A* and *B*), resulting in longer mitosis (*SI Appendix*, Fig. 3*A*). Interestingly, it did not affect the progression of the other phases of mitosis (Fig. 3*B*). This is consistent with our observation that cells dividing on soft ECM undergo delayed metaphase (Fig. 1 *F* and *G*) and display low levels of SUN2 expression (Fig. 2 *B–D*). To explore this metaphase delay further, we imaged cells stably expressing tubulin and histone 2B. In addition to the anaphase onset delay also observed in these cells (two distinct siRNAs; *SI Appendix*, Fig. 3 *B–D*), we found that cells transfected with SUN2 siRNA display an increased length of the mitotic spindle interpolar microtubules (Fig. 3 *C* and *D* and *SI Appendix*, Fig. 3 *E* and *F*), whereas we observed no significant difference in the proportion of cells with back-of-spindle chromosomes (*SI Appendix*, Fig. 3*G*). The integrity of chromosome segregation is ensured by the spindle assembly checkpoint (SAC), which delays the onset of anaphase in response to incomplete or incorrect chromosome–microtubule attachment (21). To test whether the metaphase delay we observed was SAC-dependent, we investigated the localization of MAD2, an essential SAC protein. Using a kinetochore marker (CREST) and cells stably expressing fluorescent MAD2 and histone 2B, we analyzed MAD2 localization at kinetochores in fixed cells in metaphase. We observed a significant increase in the number of MAD2-positive kinetochores in SUN2 knockdown cells compared with control cells (Fig. 3 *E* and *F*). Since chromosome congression was completed in these cells, as chromosomes were aligned at the equatorial plate, our results indicate that SUN2 depletion causes activation of the SAC in cells in metaphase. This has been observed by others when mitotic spindle defects lead to incorrect attachment or lack of tension within the kinetochores during metaphase (22). We next depleted MAD2 to inactivate the SAC and observed that SUN2 knockdown did not affect metaphase duration in MAD2-depleted cells compared with MAD2-containing cells, indicating that SUN2 depletion causes a SAC-dependent metaphase delay (Fig. 3*G* and *SI Appendix*, Fig. 3 *H* and *I*).

In interphase, SUN2 resides in the INM but its distribution after NEBD remains poorly described. We fixed HeLa cells in different stages of mitosis (Fig. 3 *H–K* and *SI Appendix*, Figs. 3*J* and 4 *A–C*) and observed that SUN2 was enriched at the spindle poles but not restricted to this polar region during metaphase (Fig. 3 *H–K* and *SI Appendix*, Fig. 3*J*). Live imaging confirmed this observation; during metaphase, DS-SUN2-GFP displayed a more intense fluorescence around the spindle poles (*SI Appendix*, Fig. 4*D*).

Taken together, these observations reinforced the idea that SUN2 plays a role to maintain mitotic spindle geometry and prompted us to investigate the mechanisms known to regulate mitotic spindle architecture.
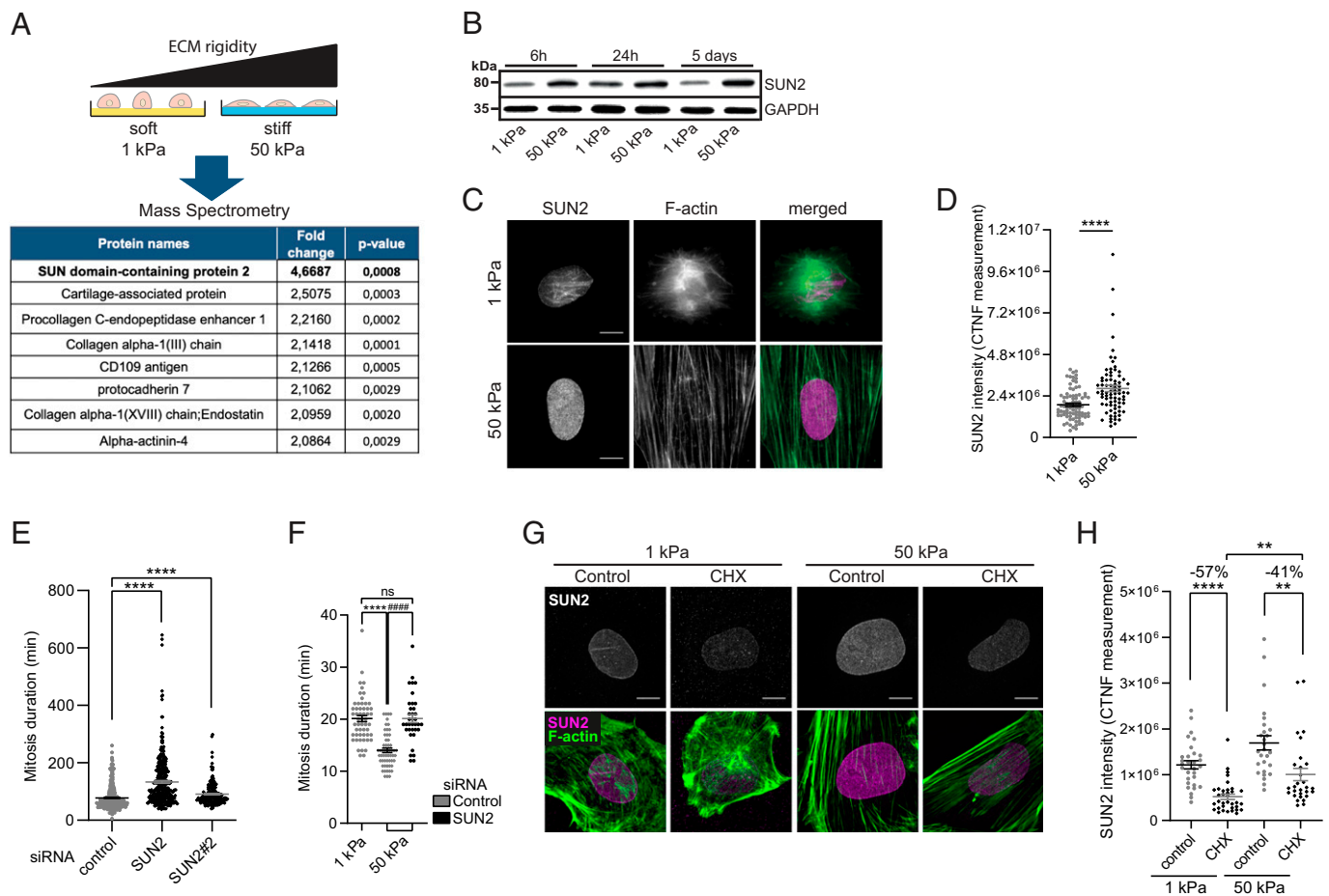
Fig. 2. SUN2 stabilization regulates mitosis duration in response to ECM rigidity. (*A*) Experimental design and schematic diagram of the workflow used in this study. A7R5 cells were cultured on soft (1 kPa) and stiff (50 kPa) polyacrylamide hydrogels for 24 h. After purification, the detergent-insoluble proteomic content was analyzed using label-free mass spectrometry and the fold change (ratio of the protein level 50 kPa/1 kPa) was calculated. Four biological replicates were generated per condition and analyzed using Welch's *t* tests, comparing the measured abundances for each peptide between 1 and 50 kPa. (*B*) A7R5 cells were cultured on soft (1 kPa) and stiff (50 kPa) polyacrylamide hydrogels for 6 h, 24 h, and 5 d. SUN2 expression was then analyzed using Western blot. Results are representative of four independent experiments. (*C*) A7R5 cells were cultured on soft (1 kPa) and stiff (50 kPa) polyacrylamide hydrogels for 24 h. After fixation, SUN2 expression was analyzed using IF (magenta) and F-actin was stained with phalloidin (green). (Scale bars, 10 μm.) (*D*) Corresponding quantifications of SUN2 intensity from *Z* stack confocal images (*n* = 84 cells for 1 kPa; *n* = 77 cells for 50 kPa; from four independent experiments; error bars indicate means ± SEM; ****P < 0.0001, Mann–Whitney *U* test). (*E*) HeLa cells depleted for SUN2 were cultured on plastic, and mitosis duration was calculated using phase-contrast microscopy (*n* = 394 cells for control siRNA and *n* = 373 cells for SUN2 siRNA from five independent experiments; *n* = 215 cells for SUN2#2 siRNA from two independent experiments; error bars indicate means ± SEM; ****P < 0.0001, Kruskal–Wallis test, Dunn's multiple-comparisons posttest). (*F*) A7R5 cells depleted for SUN2 were cultured on soft (1 kPa) and stiff (50 kPa) polyacrylamide hydrogels for 24 h. Mitosis duration was calculated using phase-contrast microscopy (*n* = 54 cells for 1-kPa control siRNA; *n* = 56 cells for 50-kPa control siRNA; *n* = 36 cells for 50-kPa SUN2 siRNA; from three independent experiments; error bars indicate means ± SEM; ns, not significant; ****P or ####P < 0.0001, Kruskal–Wallis test, Dunn's multiple-comparisons posttest). (*G*) A7R5 cells were cultured on soft (1 kPa) and stiff (50 kPa) polyacrylamide hydrogels and treated with CHX for 12 h. After fixation, SUN2 expression was analyzed using IF (magenta) and F-actin was stained with phalloidin (green). (Scale bars, 10 μm.) (*H*) Corresponding quantifications of SUN2 intensity from *Z* stack confocal images (*n* = 30 cells for 1 kPa; *n* = 35 cells for 1 kPa + CHX; *n* = 27 cells for 50 kPa; *n* = 29 cells for 50 kPa + CHX; from one experiment; error bars indicate means ± SEM; **P < 0.01, ****P < 0.0001, Kruskal–Wallis test, Dunn's multiple-comparisons posttest).

SUN2 Depletion Causes Astral Microtubule Defects. Mitotic spindle length is regulated by many factors including microtubule dynamics and cell shape (23–25). To test if SUN2 depletion affects cortical actomyosin, we monitored cortex formation in live cells undergoing mitosis and in fixed cells synchronized with STC using confocal imaging. Analysis of cell midsections did not reveal any effect of SUN2 depletion on actin cortical recruitment (Fig. 4 *A–D* and *SI Appendix*, Fig. 5*A*). Phosphorylation-dependent activation of the RhoA GEF ECT2 was reported to play a key role in triggering the recruitment of cortical actin during prophase by promoting formin-mediated actin polymerization and myosin activation (26, 27). We analyzed ECT2 phosphorylation using phosphate-affinity gel electrophoresis. As expected, we observed an increase in ECT2 phosphorylation during prometaphase (*SI Appendix*, Fig. 5*B*) and SUN2 depletion did not alter ECT2 phosphorylation in mitosis (*SI Appendix*, Fig. 5*B*).

We next assessed the effect of SUN2 depletion on microtubule dynamics and found that cells depleted for SUN2 displayed a significant decrease in astral microtubules (Fig. 4 *E* and *F*), while we observed no difference in γ-tubulin or pericentrin localization (Fig. 4 *G* and *H*). Consistent with that, we found that cells dividing on soft ECM have fewer astral microtubules compared with cells on stiff substrates (Fig. 4 *I* and *J*). To investigate how SUN2 could contribute to astral microtubule formation, we performed immunoprecipitation of SUN2 in cells synchronized with STC. We found that SUN2 interacts with cylindromatosis (CYLD) protein specifically in mitosis and not in interphase (Fig. 4*K*). CYLD is a deubiquitinase that promotes microtubule stability due to the presence of three Cap-Gly domains in its amino terminus (28). It has recently been reported that CYLD contributes to mitosis progression and localizes at the polar regions of the mitotic spindle (29) in a similar fashion as what we observed for SUN2. Interestingly,
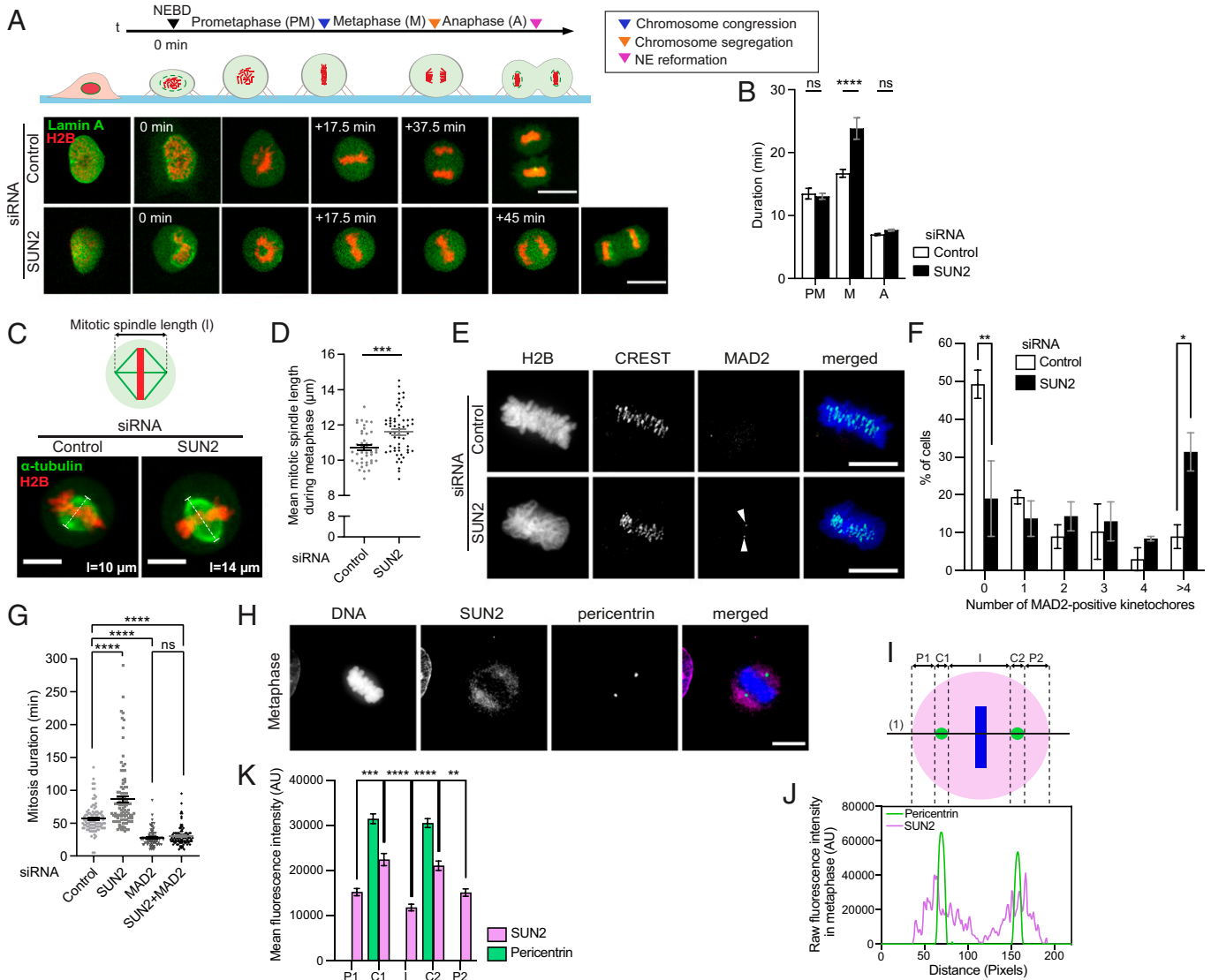
Fig. 3. SUN2 depletion causes metaphase delay and mitotic spindle defects. (A) HeLa Kyoto EGFP-LaminA/H2B-mCherry cells cultured on glass were depleted for SUN2 and imaged using live confocal microscopy. The duration of of each mitosis stage was calculated using the NEBD, shown by lamin A staining (green), as the starting point. The diagram represents the method used to calculate the phases of mitosis. (Scale bars, 20 μm.) (B) Corresponding quantifications of mitotic phase duration: prometaphase (PM), metaphase (M), and anaphase (A) ($n = 101$ cells for control siRNA and $n = 107$ cells for SUN2 siRNA from three independent experiments; error bars indicate means ± SEM; ns, not significant; ****$P < 0.0001$, two-way ANOVA, Sidak's multiple-comparisons posttest). (C) HeLa Kyoto EGFP-α-tubulin/H2B-mCherry cells cultured on glass were depleted for SUN2 and imaged using live confocal microscopy, and mean mitotic spindle length was calculated from the onset of metaphase to the image just before the onset of anaphase. The diagram represents the method used to calculate mitotic spindle length. (Scale bars, 10 μm.) (D) Corresponding quantifications of mean mitotic spindle length were calculated over metaphase duration ($n = 42$ cells for control siRNA and $n = 56$ cells for SUN2 siRNA from three independent experiments; error bars indicate means ± SEM; ***$P < 0.001$, unpaired t test). (E) HeLa Kyoto Mad2-LAP/H2B-mCherry cells cultured on glass were depleted for SUN2 and immunostained for centromeres (CREST). Representative images show the stainings of histone H2B (blue), CREST (green), and MAD2 (red). The white arrowheads show MAD2 staining. (Scale bars, 10 μm.) (F) Corresponding quantifications of the percentage of cells with MAD2-positive kinetochores ($n = 50$ cells for control siRNA and $n = 49$ cells for SUN2 siRNA from two independent experiments; error bars indicate means ± SEM; *$P < 0.05$, **$P < 0.01$, two-way ANOVA, Sidak's multiple-comparisons posttest). (G) HeLa cells cultured on plastic were transfected either with control, SUN2, MAD2, or both SUN2 and MAD2 siRNAs. Mitosis duration was calculated using phase-contrast microscopy as the elapsed time between the onset of rounding and the first image demonstrating cytokinesis and postmitotic spreading ($n = 100$ cells for each condition from two independent experiments; error bars indicate means ± SEM; ns, not significant; ****$P < 0.0001$, one-way ANOVA, Tukey's multiple-comparisons posttest). (H) HeLa cells cultured on glass were fixed and immunostained for SUN2 (magenta) and pericentrin (green). DNA was stained with DAPI (blue). Pictures of cells in metaphase were taken. (Scale bar, 10 μm.) (I) Raw fluorescence intensity profiles of SUN2 and pericentrin were plotted along the line drawn between the centrosomes in metaphase (1). The mean SUN2 fluorescence intensity was measured in the following areas delimited by pericentrin fluorescence intensity: peripheral (P1 and P2), at the centrosome (C1 and C2), and interpolar (I). (J) Representative fluorescence intensity profile of SUN2 and pericentrin in metaphase. AU, arbitrary units. (K) Mean fluorescence intensity of SUN2 and pericentrin in metaphase in the areas delimited by pericentrin staining ($n = 44$ cells from two independent experiments; error bars indicate means ± SEM; ****$P < 0.0001$, ***$P < 0.001$, **$P < 0.01$, Kruskal–Wallis test, Dunn's multiple-comparisons posttest performed for SUN2 mean fluorescence intensity).

its depletion causes metaphase delay and decreases astral microtubule stability (29). We next tested if SUN2 depletion could affect CYLD expression and observed that SUN2-depleted cells displayed less CYLD in mitosis but not in interphase (Fig. 4L), while SUN1 depletion had no effect on CYLD expression (*SI Appendix,* Fig. 5C). Consistent with these results, we observed that CYLD expression was decreased in cells undergoing mitosis on soft ECM compared with more rigid substrates (*SI Appendix,* Fig. 5D), while inhibition of CYLD did not affect SUN2 expression (*SI Appendix,* Fig. 5E). Taken together, these results indicate that low levels of SUN2 expression, due to siRNA-mediated depletion or adhesion on soft ECM, lead to a decrease in CYLD during mitosis, which in turn causes astral microtubule defects and metaphase delay.
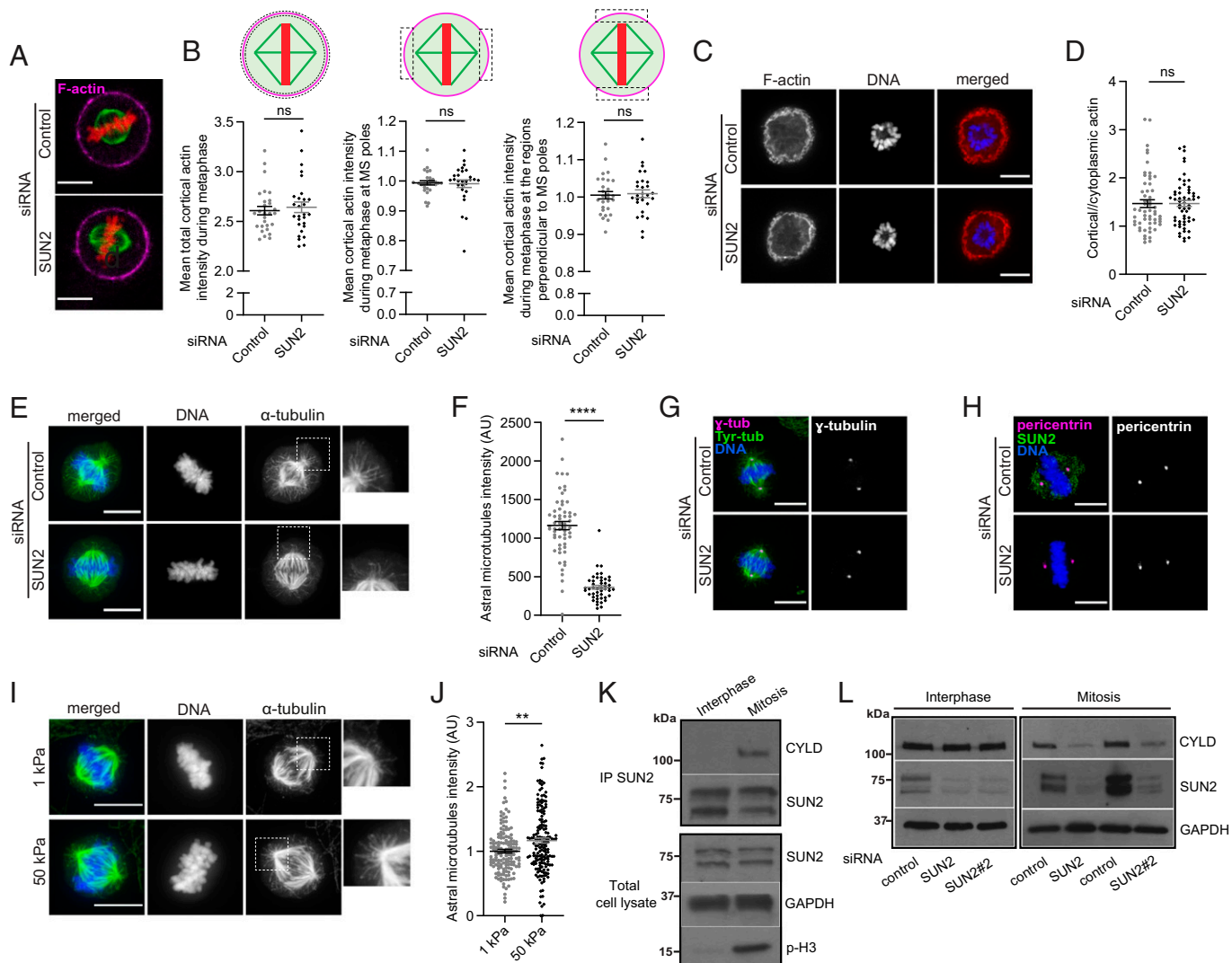
Fig. 4. SUN2 depletion causes astral microtubule defects. (*A*) HeLa Kyoto HeLa Kyoto EGFP-α-tubulin/H2B-mCherry cells depleted for SUN2 were treated with SiR-actin probe labeling F-actin (magenta) and imaged using live confocal microscopy. (Scale bars, 10 μm.) (*B*) Mean total cortical actin intensity, cortical actin intensity at mitotic spindle (MS) poles, and cortical actin intensity at regions perpendicular to MS poles were measured as shown by the dotted areas on the diagrams over metaphase duration (*n* = 28 cells for control and SUN2 siRNA from three independent experiments; error bars indicate means ± SEM; ns, not significant; Mann–Whitney *U* test). (*C*) HeLa cells depleted for SUN2 were synchronized in mitosis with STC and fixed, and F-actin was stained with phalloidin (red). DNA was stained with DAPI (blue). (Scale bars, 10 μm.) (*D*) Cortical/cytoplasmic actin ratio was quantified (*n* = 56 cells for control siRNA and *n* = 57 cells for SUN2 siRNA from one experiment; error bars indicate means ± SEM; ns, not significant; Mann–Whitney *U* test). (*E*) HeLa cells cultured on glass were depleted for SUN2, fixed, and immunostained for α-tubulin (α-tub) (green). DNA was stained with DAPI (blue). (Scale bars, 10 μm.) (*F*) Corresponding quantifications of astral microtubule intensity (*n* = 58 cells for control siRNA and *n* = 47 cells for SUN2 siRNA; error bars indicate means ± SEM; ****$P < 0.0001$, Mann–Whitney *U* test). (*G*) HeLa cells cultured on glass were depleted for SUN2, fixed, and immunostained for γ-tubulin (γ-tub) (magenta) and tyrosinated tubulin (Tyr-tub) (green). DNA was stained with DAPI (blue). (Scale bars, 10 μm.) (*H*) HeLa cells cultured on glass were depleted for SUN2, fixed, and immunostained for SUN2 (green) and pericentrin (magenta). DNA was stained with DAPI (blue). (Scale bars, 10 μm.) (*I*) HeLa cells cultured on soft (1 kPa) and stiff (50 kPa) polyacrylamide hydrogels were fixed and immunostained for α-tubulin (α-tub) (green). DNA was stained with DAPI (blue). (Scale bars, 10 μm.) (*J*) Corresponding quantifications of astral microtubule intensity (*n* = 150 cells for 1 kPa and *n* = 172 cells for 50 kPa from three independent experiments; error bars indicate means ± SEM; **$P < 0.01$, Mann–Whitney *U* test). (*K*) HeLa cells were synchronized in mitosis with STC, SUN2 immunoprecipitation (IP) was performed, and the interaction with CYLD was analyzed by Western blot (*n* = 4 independent experiments). (*L*) HeLa cells transfected with control, SUN2, or SUN2#2 siRNAs were synchronized in mitosis with STC. SUN2 and CYLD expressions were analyzed by Western blot (*n* = 4 independent experiments).

Conclusions. Our results reveal a molecular mechanism which controls mitotic progression in response to changes in tissue mechanics. We found that ECM rigidity regulates SUN2 stability, which in turn impacts mitotic progression. When cells adhere to stiff ECM, high levels of SUN2 expression promote metaphase-to-anaphase transition, whereas on soft ECM, low levels of SUN2 expression perturb astral microtubule organization and delay the onset of anaphase.

Discussion

ECM stiffness has been shown to regulate cell proliferation by promoting gene expression (30) and S phase entry in the cell cycle (8). Here, we demonstrate that cells grown on a stiff ECM undergo mitosis faster than cells grown on a soft substrate.

We found that ECM stiffness affects mitosis progression by controlling the expression of the nuclear envelope protein SUN2. SUN2 expression increases with ECM stiffness, which is consistent with previous work reporting that levels of expression of nucleoskeletal proteins including SUN2 and lamin A/C scale with tissue elasticity (31). We showed that an increase in SUN2 stability contributes to this effect. It has been proposed that SUN2 targeting to the INM follows a diffusion–retention model (32). According to this model, INM proteins distribute by free diffusion within the continuous membranes of the endoplasmic reticulum, outer

nuclear membrane, and INM, where they accumulate depending on their interactions with local protein partners. Interestingly, cells display an increased number of perinuclear actin filaments when they adhere to rigid surfaces (33). These actin filaments are connected to nesprins whose interaction with SUN2 may promote its stabilization when cells are cultured on stiff ECM.

Previous studies have explored the consequences of LINC complex alteration during mitosis, either by codepleting SUN1 and SUN2 (17, 34) or by expressing a dominant-negative KASH domain–containing protein (34). These studies reported that altering the LINC complex perturbs the cytoskeleton dynamics during prophase (17, 34), while we found that depleting SUN2 does not affect prophase but instead impacts metaphase. Kutay and colleagues also reported mitotic spindle defects in double-knockdown cells (17), which are consistent with the defects observed in SUN2-depleted cells here. This suggests that SUN1 and SUN2 may have partially redundant roles during mitosis, as it has been observed for other cellular processes (35, 36). However, whether SUN proteins interact with nesprin proteins throughout mitosis remains an open question. Our investigations indicate that low levels of SUN2 expression cause mitotic spindle and astral microtubule defects, which in turn activate the SAC and delay the onset of anaphase. Interestingly, we identified a partner of SUN2, the protein CYLD, a key regulator of microtubule dynamics (29). CYLD has been shown to be essential to maintain mitotic spindle orientation (29, 37) and CYLD depletion results in a significant reduction of astral microtubules (28) similar to the loss of astral microtubules (29) observed upon SUN2 depletion. In addition, we showed that SUN2 depletion reduces CYLD expression specifically in mitosis. We hypothesize that SUN2 could contribute to CYLD stability during metaphase. In line with this hypothesis, CYLD has been shown to be degraded as cells exit from mitosis (38), suggesting that partners like SUN2 might participate in its stabilization to maintain mitotic spindle architecture. Due to the lack of specificity of CYLD antibodies in IF experiments, we were not able to follow the dynamics of the interaction between CYLD and SUN2 during each phase of mitosis. While our results suggest that SUN2 regulates astral microtubule dynamics through CYLD, we cannot rule out that additional mechanisms may be at play. Taken together, our studies reveal a SUN2-dependent mechanism driven by ECM stiffness to regulate mitosis progression.

Materials and Methods

Cell Culture. A7R5 (ATCC CRL-1444), HeLa (ATCC CCL-2), HeLa Kyoto enhanced GFP (EGFP)–α-tubulin/H2B-mCherry (Cell Lines Service, 330670), HeLa Kyoto EGFP-LaminA/H2B-mCherry (Cell Lines Service, 330921), HeLa Kyoto Mad2-LAP/H2B-mCherry (Cell Lines Service, 330920), and MEF, a generous gift from Daniel Bouvard, Institute for Advanced Biosciences, Université Grenoble Alpes/INSERM U1209/CNRS UMR 5309 joint research center, were grown in Dulbecco's modified Eagle's medium (DMEM; Gibco) supplemented with antibiotics and 10% fetal bovine serum (Sigma-Aldrich) at 37 °C in 5% CO_2 air atmosphere.

Hydrogels with different stiffnesses coated with rat tail collagen type I were purchased from Cell Guidance Systems (Matrigen Softwell) and from Cell&Soft.

To synchronize cells in mitosis, 5 μM STC (Sigma-Aldrich, 164739) was added to the medium for 16 h and mitotic cells were then harvested by a gentle shake-off.

To test protein stability, cells were treated with 50 μg/mL CHX (Sigma-Aldrich, C7698) for 12 and 24 h; 10 μM lactacystin (Sigma-Aldrich, L6785) for 16 h; and 50 μM chloroquine (Sigma-Aldrich, C6628) for 16 h.

Cells were treated with 50 μM blebbistatin (Sigma-Aldrich, B0560) for 1 h. To inhibit CYLD, cells were treated with 30 μM subquinocin (Aobious, AOB11747) for 12 h.

Immunoblotting. Cells were washed with phosphate-buffered saline (PBS), lysed directly in Laemmli buffer (0.12 M Tris·HCl, pH 6.8, 10% glycerol, 5% sodium dodecyl sulfate [SDS], 2.5% β-mercaptoethanol, 0.005% bromophenol blue), and sonicated. Proteins were separated using 7, 10, or 12% SDS–polyacrylamide gel electrophoresis and transferred to nitrocellulose membrane. Blocking and antibody incubations were performed in Tris-buffered saline with 0.1% Tween-20 + 5% bovine serum albumin (Table 2). Detection was performed using horseradish peroxidase (HRP)–conjugated secondary antibodies (Table 3) with Clarity ECL Substrate (Bio-Rad). Membranes were imaged on a ChemiDoc XRS+ System (Bio-Rad).

Phosphate affinity gel electrophoresis was performed using Phos-tag AAL-107 (Nard Institute and Wako Pure Chemicals) according to the manufacturer's instructions (https://www.phos-tag.com/pdf/AAL-107_v12.pdf).

qRT-PCR. Total RNA was purified from cells using TRIzol reagent (MAN0001271, Ambion, Thermo Fisher Scientific) and an RNAqueous-Micro Kit (Thermo Fisher Scientific, AM1931) according to the manufacturer's instructions. RNA (1 μg) was reverse-transcribed into complementary DNA. Real-time qPCR was conducted on a 7900HT Fast Real-Time PCR System (Applied Biosystems) using TaqMan Master Mix (Applied Biosystems) and TaqMan primers/probes for *SUN2* (Rn01505183_m1) and *GAPDH* (Rn01775763_g1) according to the manufacturer's recommendations. Expression data were normalized to a standard curve generated from a pool of control cells. *GAPDH* was used as the reference gene.

Immunofluorescence. Unless stated otherwise, the cells were washed with PBS, fixed with 4% paraformaldehyde for 15 min, washed with PBS, and permeabilized for 15 min with 0.1% Triton X-100 in 1× PBS at room temperature. Cells were then washed with PBS and blocked with a blocking solution (2.5% bovine serum albumin in PBS, 0.2% Tween-20) for 45 min at room temperature. Samples were incubated overnight at 4 °C with primary antibody (Table 2) in blocking solution, followed by three washes in PBS, 0.2% Tween-20. Cells were then incubated with secondary antibody (Table 3) at room temperature for 1 h followed by three washes in PBS, 0.2% Tween-20 and two washes in PBS. Samples were mounted using ProLong Diamond Antifade Mountant with DAPI (Thermo Fisher Scientific, P36962).

For tubulin and centromere staining, the cells were washed with PBS at 37 °C followed by fixation and permeabilization with ice-cold methanol for 10 min at −20 °C. The staining was then performed using the above protocol.

Table 1. Reagents

Reagent	Company	Catalog no.	Working concentration
STC	Sigma-Aldrich	164739	5 μM
CHX	Sigma-Aldrich	C7698	50 μg/mL
Lactacystin	Sigma-Aldrich	L6785	10 μM
Chloroquine	Sigma-Aldrich	C6628	50 μM
Blebbistatin	Sigma-Aldrich	B0560	50 μM
Subquinocin	Aobious	AOB11747	30 μM
Texas red-X phalloidin	Thermo Fisher Scientific	T7471	1:500
SiR-Actin Kit	Cytoskeleton	CY-SC001	100 nM
Hoechst 33342	Thermo Fisher Scientific	H3570	1:10,000

Table 2. Primary antibodies

Antigen	Company	Catalog no. [clone]	Host species	Application, dilution
β-actin	Sigma-Aldrich	A5441 [AC-15]	Mouse	WB, 1:8,000
Centromere	CliniSciences	15-234-0001	Human	IF, ready-to-use
CYLD	Thermo Fisher Scientific	PA5-34630 [polyclonal]	Rabbit	WB, 1:1,000
Ect2	Santa Cruz Biotechnology	sc-1005 [polyclonal]	Rabbit	WB, 1:500
GAPDH	Santa Cruz Biotechnology	sc-166574 [H-12]	Mouse	WB, 1:5,000
GAPDH	Cell Signaling Technology	5174S [D16H11]	Rabbit	WB, 1:1,000
GFP	Santa Cruz Biotechnology	sc-9996 [B-2]	Mouse	WB, 1:500
Phospho-H3 (Ser10)	Invitrogen	44-1190G [polyclonal]	Rabbit	WB, 1:2,000
MAD2	Santa Cruz Biotechnology	sc-374131 [C-10]	Mouse	WB, 1:500
Pericentrin	abcam	ab28144 (produced recombinantly)	Mouse	IF, 1:1,000
Pericentrin	abcam	ab4448 [polyclonal]	Rabbit	IF, 1:300
SUN1	abcam	ab124770 [EPR6554]	Rabbit	WB, 1:1,000
SUN2	abcam	ab124916 [EPR6557]	Rabbit	IF, 1:800
SUN2	Merck Millipore	06-1038 [polyclonal]	Rabbit	WB, 1:1,000
α-tubulin	Sigma-Aldrich	T6199 [DM1A]	Mouse	IF, 1:500
γ-tubulin	BioLegend	620902 [polyclonal]	Rabbit	IF, 1:100
Tyr-tubulin	Produced from Wehland et al. (39)	Clone [YL1/2] epitope mapped to the residues (EGEEF)	Rat	IF, 1:4,000

To stain cortical actin, Texas red-X phalloidin diluted 1:500 (Thermo Fisher Scientific, T7471) was used on fixed samples. Live cells were incubated with 100 nM SiR-actin (Table 1) diluted in cell-culture medium for 10 h and washed with new medium before live confocal imaging.

siRNAs. Cells were transfected using Lipofectamine RNAiMAX reagent (Invitrogen) according to the manufacturer's instructions (protocol publication no. MAN0007825 Rev.1.0) with the following siRNAs:

SUN2 rat [Unc84bRSS342353(3_RNAI), Invitrogen]:

Forward (Fw): 5′-GAC UCG GAA GAC CUA UUC AAG AAG A-3′
Reverse (Rv): 5′-U CUU CUU GAA UAG GUC UUC CGA GUC-3′

SUN2 human: SASI_Hs01_00176980 (Sigma-Aldrich)
SUN2#2 human: *Silencer* Select Predesigned s24467 (Ambion, Thermo Fisher Scientific):

Fw: 5′-CCUUAGAGCAUGUGCCCAAtt-3′
Rv: 5′-UUGGGCACAUGCUCUAAGGta-3′

MAD2 human: *Silencer* Select Predesigned s8392 (Ambion, Thermo Fisher Scientific):

Fw: 5′-CGCCUUCGUUCAUUUACUAtt-3′
Rv: 5′-UAGUAAAUGAACGAAGGCGga-3′

MAD2#2 human: *Silencer* Select Predesigned s8393 (Ambion, Thermo Fisher Scientific):

Fw: 5′-CCUUUACUCGAGUGCAGAAtt-3′
Rv: 5′-UUCUGCACUCGAGUAAAGGtt-3′

SUN1#1 human: ON-TARGETplus siRNA (Dharmacon)

Fw: 5′-AUGUUGAAUUGGACGGCCA-3′
Rv: 5′-UGGCCGUCCAAUUCAACAU-3′

SUN1#2 human: ON-TARGETplus siRNA (Dharmacon)

Fw: 5′-GUAUAUACCAAGACGCCAU-3′
Rv: 5′-AUGGCGUCUUGGUAUAUAC-3′

Control siRNA: *Silencer* Negative Control No. 1 siRNA (AM4635 Ambion, Thermo Fisher Scientific).

Molecular Cloning. The coding sequence of *Mus musculus* SUN2 (amino acids [aa] 1 to 473) was amplified by PCR using the following primers:

Fw: 5′-TAGCTGTACAAGATGTCGAGACGAAGCC-3′
Rv: 5′-ACTAAGCTTAGTAGGGCTCTGGGTACTT-3′.

SUN2 PCR product was cloned into *Brs*GI and *Hind*III sites of a pEGFP-C1 vector to generate the DS-SUN2-GFP plasmid. The coding sequence of SUN2 (aa 1 to 473) was truncated for the SUN domain (aa 569 to 730).

To rescue SUN2 expression after 48 h of silencing, cells were washed with PBS and transfected for 24 h with DS-SUN2-GFP plasmid or control pmaxGFP plasmid (Lonza) using Lipofectamine 2000 reagent (Invitrogen) according to the manufacturer's instructions (protocol publication no. MAN0007824 Rev.1.0).

Microscopy.
Fixed samples. IF images were taken as *Z* stacks with the spinning disk confocal microscope Andromeda TILL-FEI (electron microscopy charge-coupled device [EMCCD] camera iXon 897 and α-Plan-Apochromat 63×/1.46 Oil Korr M27, WD 0.1-mm objective). Image acquisition was performed with LA, FEI software and analysis with OA, FEI software and with ImageJ.

To analyze SUN2 expression, *Z* stack images were taken of the cell height with 0.2-μm step and were processed using maximum-intensity *Z* projection on ImageJ software. The following formula was used to calculate corrected total nuclear fluorescence (CTNF) of SUN2:

$$CTNF = \text{Integrated Density} - (\text{Nuclear Area} * \text{Mean fluorescence of background readings}).$$

To analyze cortical/cytoplasmic actin ratio, images were taken on the midsection of the cell. The analysis was performed with ImageJ software by tracing a line passing through the cell center. The plot profile of actin fluorescence was then used to calculate the cortical/cytoplasmic actin ratio with the following formula:

$$\text{Cortical/cytoplasmic actin ratio} = (\text{Mean gray value intensity of the cortical actin} - \text{Mean gray value of background readings}) / (\text{Mean gray value intensity of the cytoplasmic actin} - \text{Mean gray value of background readings})$$

To analyze astral microtubule fluorescence intensity, circles were traced around the astral microtubules at each pole of the mitotic spindle and the following formula was used:

Table 3. Secondary antibodies

Secondary antibodies	Company	Catalog no. (clone)	Application, dilution
Goat anti-mouse immunoglobulin (IgG)-HRP	Santa Cruz Biotechnology	sc-2005 (polyclonal)	WB, 1:5,000
Goat anti-rabbit IgG-HRP	Santa Cruz Biotechnology	sc-2004 (polyclonal)	WB, 1:5,000
Goat anti-mouse IgG (H+L), Alexa Fluor 488	Thermo Fisher Scientific	A-11029 (polyclonal)	IF, 1:500
Goat anti-mouse IgG (H+L), Alexa Fluor 568	Thermo Fisher Scientific	A-11031 (polyclonal)	IF, 1:500
Goat anti-rabbit IgG (H+L), Alexa Fluor 568	Thermo Fisher Scientific	A-11036 (polyclonal)	IF, 1:500
Goat anti-rabbit IgG (H+L), Alexa Fluor 488	Thermo Fisher Scientific	A-11008 (polyclonal)	IF, 1:500
Cy3 AffiniPure goat anti-rat IgG (H+L)	Jackson ImmunoResearch	112-165-167 (polyclonal)	IF, 1:1,000
Goat anti-human IgG (H+L), Alexa Fluor Plus 647	Thermo Fisher Scientific	A48279TR	IF, 1:500

(Mean gray value intensity in the circle at the mitotic spindle pole − Mean gray value of background readings)/(Total mean gray value of the spindle–Mean gray value of background readings).

Live-cell imaging. For phase-contrast microscopy, live-cell imaging was performed using the Zeiss AxioObserver Z1 (CoolSnap CCD camera and Plan-Neofluar 10×/0.3 Ph1 objective) equipped with a temperature- and CO_2-controlled incubator box (37 °C and 5% CO_2). Images were taken every 5, 2.5, or 2 min for 20 h minimum. Mitosis duration was measured as the elapsed time between the onset of rounding and the first image demonstrating cytokinesis and postmitotic spreading.

Live-cell confocal imaging was performed using the spinning disk confocal microscope Andromeda TILL-FEI fitted with a Plan-Apochromat 20×/0.75, WD 610 objective and coupled to EMCCD camera iXon 897 to image HeLa Kyoto EGFP-α-tubulin/H2B-mCherry cells and HeLa Kyoto EGFP-LaminA/H2B-mCherry cells; fitted with a Plan-Apochromat 40×/1.4 Oil-DIC M27 WD 0.13 mm and coupled to EMCCD camera iXon 897 for SiR-actin labeling; and fitted with an α-Plan-Apochromat 63×/1.46 Oil Korr M27, WD 0.1-mm objective and coupled to EMCCD camera iXon 897 to image HeLa Kyoto Mad2-LAP/H2B-mCherry cells.

The microscope was equipped with a temperature- and CO_2-controlled incubator box (37 °C and 5% CO_2) and images were taken every 2.5 min for 15 h minimum. Acquisition was performed with LA, FEI software and analysis with OA, FEI software and with ImageJ.

Quantification of the duration of mitosis phases in HeLa Kyoto EGFP-LaminA/H2B-mCherry cells (Figs. 1*F* and 3*A*): Mitosis duration was calculated as the time from the first image showing NEBD to the first image showing nuclear envelope reformation. Prometaphase duration was calculated as the time from the first image showing NEBD to the last image showing all chromosome congression at the metaphase plate. Metaphase was calculated as the time from chromosome congression at the metaphase plate to the image just before chromosome segregation. Anaphase was calculated as the time from the first image showing chromosome segregation to the first image showing nuclear envelope reformation.

To quantify mitotic spindle parameters, two ImageJ macros were used: One was adapted for fixed samples and the second one for live imaging data. To quantify mitotic spindle length and metaphase plate length and width, the macro identifies the metaphase plate area by comparing the H2B (histone protein) signal with the background, the user identifies the mitotic spindle poles, and the macro calculates the pole-to-pole distance and the pole-to-metaphase plate distance.

To analyze SiR-actin labeling, an ImageJ macro was used. To quantify actin fluorescence intensity, the user identifies the mitotic spindle poles at each frame over the metaphase duration and the macro draws a line along the mitotic spindle crossing the cell membrane and finds the perpendicular to this line. The user draws lines along actin staining, crossing the line drawn between the mitotic spindle poles and the line drawn at the perpendicular. Fluorescence intensity along each line is calculated and related to the length of the line.

Statistics. Statistical analyses were performed using GraphPad Prism software. Data are presented as mean $\pm$ SEM. No exclusion criteria were used. The distribution of data (Shapiro–Wilk normality test) and the homogeneity of variances (*F* test) were tested before performing the statistical tests.

The numbers of independent experiments and the statistical tests performed for all of the quantitative data are indicated in the figure legends.

1. O. M. Lancaster *et al.*, Mitotic rounding alters cell geometry to ensure efficient bipolar spindle formation. *Dev. Cell* **25**, 270–283 (2013).
2. B. Sorce *et al.*, Mitotic cells contract actomyosin cortex and generate pressure to round against or escape epithelial confinement. *Nat. Commun.* **6**, 8872 (2015).
3. J. Folkman, A. Moscona, Role of cell shape in growth control. *Nature* **273**, 345–349 (1978).
4. J. Aureille *et al.*, Nuclear envelope deformation controls cell cycle progression in response to mechanical force. *EMBO Rep.* **20**, e48084 (2019).
5. M. Uroz *et al.*, Regulation of cell cycle progression by cell-cell and cell-matrix forces. *Nat. Cell Biol.* **20**, 646–654 (2018).
6. B. W. Benham-Pyle, B. L. Pruitt, W. J. Nelson, Mechanical strain induces E-cadherin–dependent Yap1 and β-catenin activation to drive cell cycle entry. *Science* **348**, 1024–1027 (2015).
7. S. A. Gudipaty *et al.*, Mechanical stretch triggers rapid epithelial cell division through Piezo1. *Nature* **543**, 118–121 (2017).
8. E. A. Klein *et al.*, Cell-cycle control by physiological matrix elasticity and in vivo tissue stiffening. *Curr. Biol.* **19**, 1511–1518 (2009).
9. D. E. Discher, P. Janmey, Y.-L. Wang, Tissue cells feel and respond to the stiffness of their substrate. *Science* **310**, 1139–1143 (2005).
10. D. T. Butcher, T. Alliston, V. M. Weaver, A tense situation: Forcing tumour progression. *Nat. Rev. Cancer* **9**, 108–122 (2009).
11. C. C. DuFort, M. J. Paszek, V. M. Weaver, Balancing forces: Architectural control of mechanotransduction. *Nat. Rev. Mol. Cell Biol.* **12**, 308–319 (2011).
12. N. Ramkumar, B. Baum, Coupling changes in cell shape to chromosome segregation. *Nat. Rev. Mol. Cell Biol.* **17**, 511–521 (2016).
13. S. Güttinger, E. Laurell, U. Kutay, Orchestrating nuclear envelope disassembly and reassembly during mitosis. *Nat. Rev. Mol. Cell Biol.* **10**, 178–191 (2009).
14. M.-Y. Tsai *et al.*, A mitotic lamin B matrix induced by RanGTP required for spindle assembly. *Science* **311**, 1887–1893 (2006).
15. A. V. Orjalo *et al.*, The Nup107-160 nucleoporin complex is required for correct bipolar spindle assembly. *Mol. Biol. Cell* **17**, 3806–3818 (2006).
16. R. W. Wong, G. Blobel, E. Coutavas, Rae1 interaction with NuMA is required for bipolar spindle formation. *Proc. Natl. Acad. Sci. U.S.A.* **103**, 19783–19787 (2006).
17. Y. Turgay *et al.*, SUN proteins facilitate the removal of membranes from chromatin during nuclear envelope breakdown. *J. Cell Biol.* **204**, 1099–1109 (2014).
18. V. Nunes *et al.*, Mechanosensitive nuclear asymmetries define a bipolar spindle scaffold to ensure mitotic fidelity. *bioRxiv* [Preprint] (2019). https://doi.org/10.1101/526939. Accessed 26 October 2022.
19. B. D. Hoffman, C. Grashoff, M. A. Schwartz, Dynamic molecular processes mediate cellular mechanotransduction. *Nature* **475**, 316–323 (2011).
20. D. Mitrossilis *et al.*, Single-cell response to stiffness exhibits muscle-like behavior. *Proc. Natl. Acad. Sci. U.S.A.* **106**, 18243–18248 (2009).
21. A. Amon, The spindle checkpoint. *Curr. Opin. Genet. Dev.* **9**, 69–75 (1999).
22. N. London, S. Biggins, Signalling dynamics in the spindle checkpoint response. *Nat. Rev. Mol. Cell Biol.* **15**, 736–747 (2014).
23. S. Dumont, T. J. Mitchison, Force and length in the mitotic spindle. *Curr. Biol.* **19**, R749–R761 (2009).
24. S. L. Prosser, L. Pelletier, Mitotic spindle assembly in animal cells: A fine balancing act. *Nat. Rev. Mol. Cell Biol.* **18**, 187–201 (2017).

25. P. Kunda, B. Baum, The actin cytoskeleton in spindle assembly and positioning. *Trends Cell Biol.* **19**, 174–179 (2009).
26. A. Rosa, E. Vlassaks, F. Pichaud, B. Baum, Ect2/Pbl acts via Rho and polarity proteins to direct the assembly of an isotropic actomyosin cortex upon mitotic entry. *Dev. Cell* **32**, 604–616 (2015).
27. S. P. Ramanathan *et al.*, Cdk1-dependent mitotic enrichment of cortical myosin II promotes cell rounding against confinement. *Nat. Cell Biol.* **17**, 148–159 (2015).
28. Y. Yang, J. Zhou, CYLD–A deubiquitylase that acts to fine-tune microtubule properties and functions. *J. Cell Sci.* **129**, 2289–2295 (2016).
29. Y. Yang *et al.*, CYLD regulates spindle orientation by stabilizing astral microtubules and promoting dishevelled-NuMA-dynein/dynactin complex formation. *Proc. Natl. Acad. Sci. U.S.A.* **111**, 2158–2163 (2014).
30. M. Aragona *et al.*, A mechanical checkpoint controls multicellular growth through YAP/TAZ regulation by actin-processing factors. *Cell* **154**, 1047–1059 (2013).
31. J. Swift *et al.*, Nuclear lamin-A scales with tissue stiffness and enhances matrix-directed differentiation. *Science* **341**, 1240104 (2013).
32. R. Ungricht, M. Klann, P. Horvath, U. Kutay, Diffusion and retention are major determinants of protein targeting to the inner nuclear membrane. *J. Cell Biol.* **209**, 687–703 (2015).
33. D. B. Lovett, N. Shekhar, J. A. Nickerson, K. J. Roux, T. P. Lele, Modulation of nuclear shape by substrate rigidity. *Cell. Mol. Bioeng.* **6**, 230–238 (2013).
34. A. J. R. Booth *et al.*, Contractile acto-myosin network on nuclear envelope remnants positions human chromosomes for mitosis. *eLife* **8**, e46902 (2019).
35. K. Lei *et al.*, SUN1 and SUN2 play critical but partially redundant roles in anchoring nuclei in skeletal muscle cells in mice. *Proc. Natl. Acad. Sci. U.S.A.* **106**, 10207–10212 (2009).
36. Q. Liu *et al.*, Functional association of Sun1 with nuclear pore complexes. *J. Cell Biol.* **178**, 785–798 (2007).
37. S. Xie *et al.*, CYLD deficiency promotes pancreatic cancer development by causing mitotic defects. *J. Cell. Physiol.* **234**, 9723–9732 (2019).
38. F. Stegmeier *et al.*, The tumor suppressor CYLD regulates entry into mitosis. *Proc. Natl. Acad. Sci. U.S.A.* **104**, 8869–8874 (2007).
39. J. Wehland, H. C. Schröder, K. Weber, Amino acid sequence requirements in the epitope recognized by the alpha-tubulin-specific rat monoclonal antibody YL 1/2. *EMBO J.* **3**, 1295–1300 (1984).
40. N. Belaadi *et al.*, Data from SUN2 regulates mitotic duration in response to extracellular matrix rigidity. Dryad. https://doi.org/10.5061/dryad.ns1rn8pvv. Deposited 17 October 2022.